INTERNATIONAL JOURNAL FOR NUMERICAL METHODS IN FLUIDS
Int. J. Numer. Meth. Fluids 2006; **51**:351–369
Published online 18 April 2006 in Wiley InterScience (www.interscience.wiley.com). DOI: 10.1002/fld.982

Generalized lattice-BGK concept for thermal and chemically reacting flows at low Mach numbers

D. Hänel*,†, U. Lantermann, R. Kaiser and I. Wlokas

Institute of Combustion and Gasdynamics, University of Duisburg-Essen, D-47048 Duisburg, Germany

SUMMARY

The lattice-BGK method has been extended by introducing additional, free parameters in the original formulation of the lattice-BGK methods. The relationship between these parameters and the macroscopic moment equations is analysed by Taylor series and Chapman–Enskog expansion. The parameters are determined from the macroscopic moment equations by comparisons with the governing equations to be modelled. Extensions are presented for the Navier–Stokes equations at low Mach numbers in Cartesian or axisymmetric coordinates with constant or variable density, for scalar convection–diffusion equations and for equations of Poisson type. The generalized lattice-BGK concept is demonstrated by two applications of chemical engineering. These are the computation of chemically reacting flow through an axisymmetric reactor and of the transport and deposition of particles to filters under the action of different forces.

KEY WORDS: lattice-BGK method; axisymmetric; low Mach number; variable density

1. INTRODUCTION

Thermal and chemically reacting flows at low Mach numbers are typical flow problems in chemical engineering, where compressibility effects are small but density changes are large due to heat transfer or chemical heat release. Such problems are characterized by different physical effects. The characteristic scales differ often by orders of magnitudes, resulting in mathematically stiff governing equations. Examples for that are the acoustic and flow scales at low Mach numbers or the chemical relaxation times and flow times in reactive flows. Computations of such flow problems are expensive in most cases, in particular if complex geometry and boundary conditions exist in addition. An alternative solution concept to usual

*Correspondence to: D. Hänel, Institute of Combustion and Gasdynamics, University of Duisburg-Essen, D-47048 Duisburg, Germany.
†E-mail: haenel@ivg.uni-duisburg.de

Contract/grant sponsor: German Research Society (DFG)

Received 28 October 2004
Revised 4 March 2005
Accepted 5 March 2005

conventional CFD methods offer the lattice-Boltzmann (LB) methods, which avoid or at least reduce some of the difficulties in stiff problems.

The concept of LB models is based, in principle, on the lattice gas or cellular automata, described e.g. in Reference [1]. LB methods as independent numerical methods for fluid-dynamic simulations were introduced by McNamara *et al.* [2]. The Boolean algebra was replaced here by continuous velocity distributions to avoid the statistical noise of cellular automata. Enhanced collision formulations and tuning of the viscosity were introduced by Higuera *et al.* [3, 4]. An efficient variant of these LB models is the lattice-BGK (LBGK) method, published in the early 1990s by Qian *et al.* [5] and Chen *et al.* [6]. The success of the LBGK concept is essentially based on the use of the so-called BGK collision operator, where the molecular distribution function relaxes to its equilibrium value. Details of the LBGK concept, as used here, are given in Section 3. The discrete phase space of LBGK methods is given in the form of Cartesian-like lattices, therefore they behave like Cartesian grid solvers for solving the Navier–Stokes equations. General advantages of Cartesian grid solvers are the easy grid generation and the simple algorithmic structures. However, additional algorithmic developments are required in the case of anisotropic flow fields and for complex geometries with curved boundaries. Corresponding developments for LBGK methods are published by the authors, so for local grid refinement, e.g. in Reference [7], for higher order boundary approximations on curvilinear contours in Reference [8] or for acceleration strategies using grid refinement [9]. The inherent, small time steps of the LBGK methods, scaled with the isothermal speed of sound c_s, and the local grid refinement make the LBGK methods to efficient solution concepts for mathematically stiff flow problems. The method is additionally characterized by simple and granular algorithms, well suited for efficient parallelization. However, the classical formulation is not sufficient for many practical, physical or geometrical cases as, e.g. for reactive flows at low Mach numbers or for axisymmetric flow configurations. Attempts were made to generalize the grid concept to unstructured grids, e.g. in Reference [10] or Reference [11]. Our experiences with LBGK methods based on finite volumes, e.g. in Reference [12], were not so positive, since the methods loose their essential advantage of simple algorithm and high accuracy.

Aim of the present study is therefore to extend the LBGK concept to more general applications but to preserve the favourable properties of this gas-kinetic concept on isotropic Cartesian-like meshes. Extensions are made in this study by introducing additional free parameters to the LBGK formulation, which are determined by comparisons of the corresponding moment equations with the flow equations under consideration as shown in Section 4. Examples for such extensions are the Navier–Stokes equations in Cartesian or axisymmetric coordinates with constant or variable density (low Mach number approximation), scalar convection–diffusion equations and Poisson equations. The applicability of this LBGK concept is demonstrated by a computation of chemically reacting flow in an axisymmetric reactor and by the simulation of particle transport and deposition. Comparisons are made with corresponding finite-difference solutions.

2. LOW MACH NUMBER APPROXIMATION OF NAVIER–STOKES EQUATIONS

An important class of fluid-dynamic problems are flows at low Mach numbers but variable density. The Navier–Stokes equations for compressible fluids and incompressible fluids, as

well, are not or only conditionally suited for computing this class of flows. Typical examples are flows through chemical reactors or heat exchangers usually at low speeds. Variations of the density are caused in these cases either internally by heat release of chemical reactions or externally by wall heating, but not by compression of the gas. This situation is characterized by a low Mach number $Ma = U/a_\infty \ll 1$. The acoustic speed of sound a_∞ is much larger then a typical flow velocity U. Hence, one consequence is that the Navier–Stokes equations of compressible fluids become a mathematically stiff system and converge only slowly due to the very different time scales. Another consequence is a spatially constant thermodynamic pressure $p_{\text{therm}} = \rho RT \approx p_{\text{therm}}(t)$. The situation is consequently modelled by a scale analysis of the Navier–Stokes equations for compressible fluids with respect to small Mach numbers, discussed e.g. in References [13, 14]. The analysis is based on the non-dimensional Navier–Stokes equations for compressible fluids with non-dimensional velocities referenced by U, the pressure by $p_{\text{ref}} = \rho_{\text{ref}} RT_{\text{ref}}$ and with a reference length L and viscosity μ_{ref}. The non-dimensional momentum equation, using the tensor notation $\delta_\alpha f$ for $\partial f/\partial x_\alpha$ and $\delta_{\alpha\beta}$ for the Kronecker symbol, reads

$$\partial_{\tilde{t}}(\tilde{\rho}\tilde{u}_\alpha) + \partial_\beta(\tilde{\rho}\tilde{u}_\beta\tilde{u}_\alpha) + \frac{1}{\gamma Ma^2}\,\partial_\alpha\tilde{p} = \frac{1}{Re}\,\partial_\beta\tilde{\mu}\left(\partial_\beta\tilde{u}_\alpha + \partial_\alpha\tilde{u}_\beta - \frac{2}{3}\,\delta_{\alpha\beta}\partial_\gamma\tilde{u}_\gamma\right) \tag{1}$$

The dimensionless pressure is now written in a series of Mach number:

$$\tilde{p} = \tilde{p}^{(0)} + Ma\;\tilde{p}^{(1)} + Ma^2\;\tilde{p}^{(2)} \tag{2}$$

The pressure $\tilde{p}^{(0)}$ is the thermodynamic pressure, described by the gas equation $\tilde{p}^{(0)} = \tilde{\rho}\,R\,\tilde{T}$, the acoustic pressure $\tilde{p}^{(1)}$ is the pressure of weak pressure waves and $\tilde{p}^{(2)}$ is the hydrodynamic pressure responsible for the conservation of mass (as in incompressible flows). Introduction of Equation (2) in Equation (1) results in zeroth order for the limit $Ma \to 0$ to

$$\partial_\alpha\tilde{p}^{(0)} = 0 \quad \text{or} \quad \tilde{p}^{(0)} = \tilde{p}^{(0)}(t)$$

The next higher order, which leads to a non-trivial momentum equation, introduces the hydrodynamic pressure $\sim Ma^2\;\tilde{p}^{(2)}$. The consideration of the acoustic mode $\sim Ma\;\tilde{p}^{(1)}$ is neglected here. It requires additional scaling in time and space and leads to a hyperbolic system of equations for aeroacoustic applications [14].

Final result of the expansion equation (2) is the so-called *low Mach number approximation* (*LMNA*) *of the Navier–Stokes equations* [14], which is the basis for computing thermal and reacting flows at low Mach numbers. The complete set of the low Mach number approximation of the Navier–Stokes equations for thermal flows of ideal gases reads in Cartesian coordinates x_α or x_β with $\alpha = \beta = x, y, z$:

- Continuity equation:

$$\partial_t\rho + \partial_\alpha(\rho u_\alpha) = 0 \tag{3}$$

- Momentum equations:

$$\partial_t\rho u_\alpha + \partial_\beta(\rho u_\beta u_\alpha) + \partial_\alpha p^{(2)} = \partial_\beta\mu(\partial_\beta u_\alpha + \partial_\alpha u_\beta - \tfrac{2}{3}\,\delta_{\alpha\beta}\partial_\gamma u_\gamma) \tag{4}$$

  where $p^{(2)}$ is the hydrodynamic pressure, ensuring mass conservation.

- Energy equation for enthalpy $h = c_p T$:

$$\rho \partial_t h + \rho u_\beta \partial_\beta h + \frac{\mathrm{d} p^{(0)}}{\mathrm{d}t} = \partial_\gamma \lambda \partial_\gamma T \tag{5}$$

  with the thermodynamic pressure $p^{(0)}(t)$, which is a function of time only,
- Density $\rho(T)$ in thermal flows

$$\rho(\mathbf{x}, t) = \frac{p^{(0)}(t)}{R T(\mathbf{x}, t)} \tag{6}$$

Chemically reacting flows require in addition a set of species equations. An example is shown in Section 5.1.

3. LATTICE-BGK APPROACH

Aim of this section is the development of a LBGK method, which models the low Mach number approximation of the Navier–Stokes equations with variable density and other important equations of fluid dynamics in Cartesian and axisymmetric coordinate systems.

3.1. Basics of the lattice-BGK method

Starting point is the LBGK method as originally published in References [5, 6]. The method is based on Cartesian-like lattices in two and three dimensions as sketched in Figure 1.

Along each link i an amount of molecules, expressed by a discrete distribution function f_i, is moved from node to node with molecular speeds $\mathbf{c}_i$ of constant Cartesian velocity components $c_0 \gg U$. One zero speed is assumed in addition. The following definitions for the molecular speed c_0, the square modulus p and the isothermal speed of sound c_s are common:

$$c_0 \sim U/Ma \gg U \quad p = \frac{c_{i\alpha}^2}{c_0^2} \quad c_s^2 = \frac{1}{3} c_0^2$$

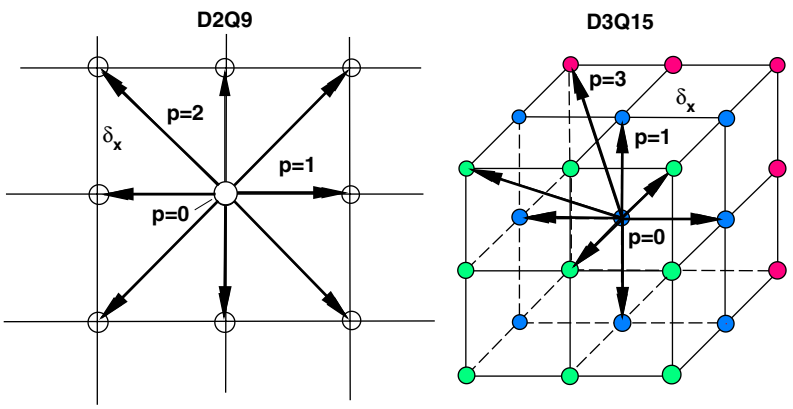

Figure 1. Discrete phase space (lattices) in two (D2Q9) and in three (D3Q15) dimensions.

The LBGK equation for the distribution function $f_i(t,\mathbf{r})$ in direction of the discrete molecular speed $\mathbf{c}_i$ reads

$$f_i(t+\delta_t,\mathbf{r}+\mathbf{c}_i\delta_t)=f_i(t,\mathbf{r})+\Omega[F_i(t,\mathbf{r})-f_i(t,\mathbf{r})]+\delta t\, s_i^{(k)} \tag{7}$$

The additional source terms

$$s_i^{(k)}=s_i^{(1)}+\delta t\, s_i^{(2)} \tag{8}$$

are determined in a later section. The dimensionless collision frequency Ω is connected with the kinematic viscosity v by the relation

$$v=\mu/\rho=\delta t\, c_s^2\left(\frac{1}{\Omega}-\frac{1}{2}\right) \tag{9}$$

The parameter Ω is a variable in space and time even for constant dynamic viscosity μ, if the density ρ is variable in space and time. The discrete equilibrium distribution F_i is derived from the Maxwellian distribution by an expansion with respect to small Mach numbers, assuming $\sqrt{u_\alpha^2/c_s^2}\ll 1$. The equilibrium distribution F_i with variable density ρ and additional correction term $F_{i,\mathrm{corr}}$ reads

$$F_i=t_p\left[\frac{P}{c_s^2}+\frac{\rho\, u_\alpha\, c_{i\alpha}}{c_s^2}+\frac{\rho\, u_\alpha\, u_\beta}{2c_s^2}\left(\frac{c_{i\alpha}c_{i\beta}}{c_s^2}-\delta_{\alpha\beta}\right)\right]+F_{i,\mathrm{corr}} \tag{10}$$

The term $F_{i,\mathrm{corr}}$ is again a correction term, determined later. The macroscopic pseudo-pressure term $P(t,\mathbf{r})$ collects diagonal elements of the stress tensor. It acts like the hydrodynamic pressure $p^{(2)}$ in the original LBGK method. The weighting factors t_p are functions of the square modulus p:

$$\begin{aligned}\text{D2Q9: } p=0,1,2 \quad t_p=4/9,1/9,1/36\\ \text{D3Q15: } p=0,1,3 \quad t_p=2/9,1/9,1/72\end{aligned} \tag{11}$$

The macroscopic, invariant moments are defined as

$$\sum_i f_i=\sum_i F_i=P/c_s^2 \tag{12}$$

and

$$\sum_i f_i c_{i,\alpha}=\sum_i F_i c_{i,\alpha}=\rho u_\alpha \tag{13}$$

The formulation of boundary conditions on the molecular level, i.e. for the distribution function, enable it to deal with complex surfaces in a relatively easy way. Widely used formulations are the 'bouncing back conditions' on rigid walls or the conditions based on the equilibrium distribution equation (10) using macroscopic boundary values. These conditions are formally first order accurate if a boundary is not aligned with the grid. An alternative formulation, used in this paper for curvilinear boundaries, is a combination of both, resulting in a second order accurate boundary formulation for arbitrary grids, published by the authors in Reference [12].

Local mesh refinement, as described in Reference [7], is used to refine zones, where smaller scale lengths, as shear layers or flame zones, have to be resolved. The grid cells are subdivided

by a refinement factor n between 2 and 10 with special transfer relations for the distribution function between coarse and fine grids. Since the size of the time step decreases with the refinement factor n, the CPU-time increases correspondingly. An essential reduction of CPU-time can be achieved for steady-state problems when using local mesh refinement together with the acceleration concept published in Reference [9].

3.2. Analysis of lattice-BGK approach

The analysis, based on Taylor series and Chapman–Enskog expansions connects the microscopic, discrete LBGK approach with the macroscopic moment equations. Aim is to incorporate the parameters $s_i^{(k)}$, $F_{i,\mathrm{corr}}$ and $P(t,\mathbf{r})$ into the moment equations. The analysis is presented in a rather compact form, more details are found, e.g. in References [15, 16].

The LBGK equation (7), expanded in space and in time by Taylor series, yields

$$D_\alpha f_i + \frac{\delta t}{2} D_\alpha D_\beta f_i = \frac{\Omega}{\delta t}(F_i - f_i) + s_i^{(1)} + \delta t s_i^{(2)} \tag{14}$$

with the abbreviation for the 'substantial' derivative

$$D_\alpha \equiv \partial_t + c_\alpha \partial_\alpha \tag{15}$$

The non-equilibrium function f_i is split in a series of perturbation distributions $f_i^{(k)}$ according to the classical Chapman–Enskog expansion

$$f_i = F_i + \delta t\, f_i^{(1)} + \delta t^2\, f_i^{(2)} + \cdots \tag{16}$$

Introduction of this series in Equation (14) under consideration of only the first perturbation $f_i^{(1)}$ results in

$$D_\alpha F_i + \frac{\delta t}{2} D_\alpha D_\beta F_i + \delta t\, D_\alpha f_i^{(1)} = -\Omega\, f_i^{(1)} + s_i^{(1)} + \delta t s_i^{(2)} \tag{17}$$

The perturbation distribution $f_i^{(1)}$ is determined from Equation (17) taking the limit $\delta t \to 0$

$$f_i^{(1)} = -\frac{1}{\Omega}\,(D_\alpha F_i - s_i^{(1)})$$

The expanded LBGK equation (14), then reads

$$D_\alpha F_i = \delta t \left(\frac{1}{\Omega} - \frac{1}{2}\right) D_\alpha D_\beta F_i - \Omega\, f_i^{(1)} - \frac{\delta t}{\Omega} D_\alpha s_i^{(1)} + s_i^{(1)} + \delta t s_i^{(2)} \tag{18}$$

The source term $s_i^{(1)}$ is assumed to be independent of the molecular speed c_α, so that $\sum_i c_\alpha s_i^{(1)} = 0$, while the second term $\sim \delta t s_i^{(2)}$ depends linearly on the molecular speed such that $\sum_i s_i^{(2)} = 0$. The moments of the perturbation distribution are, according to Equations (12) and (13), defined by

$$\sum_i f_i^{(1)} = 0 \quad \text{and} \quad \sum_i c_\alpha\, f_i^{(1)} = 0 \tag{19}$$

The macroscopic moment equations are derived from Equation (18) by summation over all molecular speeds i in Equation (18), exploring the symmetry properties of the discrete phase

space (lattices) in Figure 1. The macroscopic variables are defined by the moments equations (12) and (13) and by the definition equation (9) of the kinematic viscosity $\nu(\Omega)$.

The equation of the zeroth moment M_0 represents the mass conservation in the frame of the LBGK method and reads

$$\partial_t(P/c_s^2) + \partial_\alpha(\rho u_\alpha) - \sum_i s_i^{(1)} = O(\delta t) \tag{20}$$

The equations of the first moment M_1 are constructed in a corresponding manner by multiplication of Equation (18) with $c_{i,\alpha}$ and summation over all speeds. The moment M_1 describes the momentum conservation in the frame of the LBGK method and yields

$$\begin{aligned} &\partial_t \rho u_\alpha + \partial_\beta(\rho u_\beta u_\alpha) + \partial_\alpha P - \partial_\beta \nu[\partial_\beta(\rho u_\alpha) + \partial_\alpha(\rho u_\beta) + \delta_{\alpha\beta}\partial_\gamma(\rho u_\gamma)] \\ &= -\partial_\beta \sum_i c_\alpha c_\beta F_{i,\mathrm{corr}} - \frac{\delta t}{\Omega}\sum_i D_\alpha c_\alpha s_i^{(1)} + \delta t \sum_i c_\alpha s_i^{(2)} + O(\delta t^2) \end{aligned} \tag{21}$$

4. ADAPTED LATTICE-BGK METHODS

The macroscopic moments equations (20) and (21) of the LBGK approach are not closed due to the undefined quantities s_i, $F_{i,\mathrm{corr}}$ and P. These quantities are determined by comparisons of the macroscopic moments with the governing equations of the actual problem under consideration. A number of important examples are derived in the following.

4.1. Navier–Stokes equations of incompressible fluids in Cartesian coordinates

The Navier–Stokes equations for a fluid with constant density $\rho = \rho_0 = \mathrm{cost}$ in Cartesian coordinates $\alpha = \beta = x, y, z$ read

$$\begin{aligned} \partial_\alpha u_\alpha &= 0 \\ \partial_t u_\alpha + \partial_\beta u_\beta u_\alpha + \partial_\alpha p/\rho_0 &= \partial_\beta \nu[\partial_\beta u_\alpha + \partial_\alpha u_\beta] \end{aligned} \tag{22}$$

The LBGK method for solving the Navier–Stokes equations of incompressible fluids in Cartesian coordinates was the starting point of the consideration in Section 3. Therefore, it is expected that the source terms $s_i^{(k)}$ and the correction distribution $F_{i,\mathrm{corr}}$ are zero and that the pressure term P corresponds to the hydrodynamic pressure $p^{(2)}$. This assumption is confirmed by the comparison of the moments M_0 and M_1 in Equations (20) and (21) with the Navier–Stokes equations (22). The comparison yields

$$s_i^{(1)} = s_i^{(2)} = 0 \quad F_{i,\mathrm{corr}} = 0 \quad P = p = p^{(2)} \tag{23}$$

4.2. Navier–Stokes equations of incompressible fluids in axisymmetric coordinates

An axisymmetric formulation is much more effective than a corresponding three-dimensional computation in problems, where the assumption of axial symmetry is justified. Defining the coordinates $\alpha = \beta = x, r$, where x is the axial coordinate and r the radial coordinate, the

Navier–Stokes equations of an incompressible fluid in axisymmetric coordinates (x, r, t) is written as

$$\begin{aligned} \partial_\alpha u_\alpha + u_r/r &= 0 \\ \partial_t u_\alpha + \partial_\beta u_\beta u_\alpha + u_r u_\alpha/r + \partial_\alpha p/\rho_0 &= \partial_\beta \nu[\partial_\beta u_\alpha + \partial_\alpha u_\beta] \\ &\quad + \frac{\nu}{r}(\delta_{\alpha x}(\partial_r u_x + \partial_x u_r) + \delta_{\alpha r} 2 \cdot \partial_r(u_r/r)) \end{aligned} \tag{24}$$

with the velocities u_x and u_r in axial and radial direction.

The curvature terms $\sim 1/r$ introduce non-homogenous behaviour between the axial and radial directions, so the basic LBGK concept is not directly transferable to it. A corresponding, discrete LBGK concept for cylindrical coordinates is not known to the authors. A flexible way out to handle axisymmetry is proposed here by introducing the source terms as defined in Equation (7). The source terms are determined by comparing the equations of moments M_0 and M_1, Equations (20) and (21), with the Navier–Stokes equations (24), given above. The comparison yields

$$F_{i,\mathrm{corr}} = 0 \quad \text{and} \quad P = p = p^{(2)} \tag{25}$$

where $p^{(2)}$ is the hydrodynamic pressure. The source terms caused by curvature terms read

$$\begin{aligned} s_i^{(1)} &= -u_r/r \quad \text{if } c_{i,\alpha} = 0 \quad \text{else } s_i^{(1)} = 0 \\ s_i^{(2)} &= \frac{t_p}{c_s^2}\left[\frac{1}{r}(\partial_r u_x + \partial_x u_r)c_{i,x} + 2\partial_r(u_r/r)c_{i,r}\right] \end{aligned} \tag{26}$$

A similar derivation of a LBGK method for axisymmetric, incompressible flow is found in the literature in Reference [17].

A test case, for which an analytical solution is available, is the developed, laminar flow through an axisymmetric, concentric pipe. Figure 2 shows axial velocity profiles between inner and outer cylinder wall, computed with this LBGK method and from the analytical solution. The analytical (crosses) and the LBGK solution (full line) are nearly identically, as expected. To demonstrate the difference to the plane flow through a channel, the corresponding solution is plotted as dashed line. The comparison confirms the correct formulation of the LBGK method using the source terms of Equation (26).

4.3. Low Mach number approximation of the Navier–Stokes equations in a Cartesian frame

The low Mach number approximation of the Navier–Stokes equations with variable density is defined by the continuity and the momentum equations (3) and (4). The free parameters s_i, $F_{i,\mathrm{corr}}$ and P of the LBGK method are determined from these equations by comparison with the equations of moments, Equations (20) and (21). It yields the following

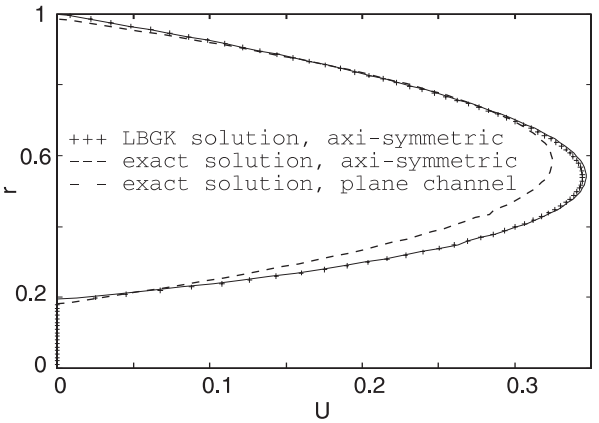

Figure 2. Axial velocity of developed pipe flow between radius $R_\mathrm{i} = 0.2$ and radius $R_\mathrm{o} = 1$. ——— Axisymmetric lattice-BGK solution. ++++ Axisymmetric analytical solution. - - - - Analytical solution of plane channel between R_i and R_o.

quantities:

$$
\begin{aligned}
s_i^{(1)} &= -\partial_t \rho \quad \text{if } c_{i,\alpha} = 0 \quad \text{else } s_i^{(1)} = 0 \\
s_i^{(2)} &= 0 \\
F_{i,\mathrm{corr}} &= t_p \nu u_\gamma \partial_\delta \rho \left(\frac{c_{i\gamma} c_{i\delta}}{c_\mathrm{s}^2} - \delta_{\gamma\delta} \right) \\
P &= p^{(2)} + \tfrac{2}{3}\, \mu \partial_\gamma u_\gamma + \nu \partial_\gamma (\rho u_\gamma)
\end{aligned}
\tag{27}
$$

The time derivative of the density $\partial_t \rho$ in the source term $s_i^{(1)}$ is approximated by a difference using the known values of ρ from the actual and from the previous time level. The distribution $F_{i,\mathrm{corr}}$ corrects the influence of the variable density ρ in the stress tensor, which arises in the moment equation (21). The pressure-like term P contains here the hydrodynamic pressure $p^{(2)}$ and additionally a stress contribution for the correct bulk viscosity term. This diagonal term has to be evaluated at the boundaries only, see Reference [16]. The resulting LBGK method agrees with the LBGK method, proposed for chemically reacting flows in Reference [16].

4.4. Low Mach number approximation in axisymmetric coordinates

An axisymmetric LBGK method for the low Mach number approximation of the Navier–Stokes equations is of interest for flow computations in devices of circular cross-sections with axisymmetric and usually stationary, thermal or reacting flows. A typical example is the chemical reactor, computed in Section 5.1.

The extension of the continuity and momentum equations (3) and (4) to axisymmetric coordinates with additional curvature terms on the right-hand side reads:

$$
\partial_t \rho + \partial_\alpha (\rho u_\alpha) = -\frac{1}{r}\, \rho\, u_r \tag{28}
$$

$$\partial_t \rho u_\alpha + \partial_\beta(\rho u_\beta u_\alpha) + \partial_\alpha p^{(2)} - \partial_\beta \mu \left(\partial_\beta u_\alpha + \partial_\alpha u_\beta - \frac{2}{3}\,\delta_{\alpha\beta}\partial_\gamma u_\gamma \right)$$

$$= \frac{1}{r}\left(-\rho u_r\, u_\alpha + \mu \left(\delta_{\alpha x}(\partial_r u_x + \partial_x u_r) + \delta_{\alpha r}\, 2 \cdot \partial_r \left(\frac{u_r}{r} \right) \right) \right) \tag{29}$$

The comparison of the governing equations (28) and (29) with the equations of moments, Equations (20) and (21), yields the following quantities:

$$\begin{aligned} s_i^{(1)} &= -\partial_t\, \rho - \rho u_r / r \quad \text{if } c_{i,\alpha} = 0 \quad \text{else } s_i^{(1)} = 0 \\ s_i^{(2)} &= \frac{t_p}{c_s^2}\left[\frac{1}{r}\,(\partial_r u_x + \partial_x u_r)\, c_{i,x} + 2\partial_r(u_r/r)\, c_{i,r} \right] \\ F_{i,\mathrm{corr}} &= t_p\, \nu u_\gamma \partial_\delta \rho \left(\frac{c_{i\gamma} c_{i\delta}}{c_s^2} - \delta_{\gamma\delta} \right) \\ P &= p^{(2)} + \tfrac{2}{3}\,\mu\, \partial_\gamma u_\gamma + \nu \partial_\gamma(\rho u_\gamma) \end{aligned} \tag{30}$$

The source terms $s_i^{(1)}$ and $s_i^{(2)}$ contain again the curvature terms $\sim 1/r$, the meaning of the quantities P and $F_{i,\mathrm{corr}}$ remains unchanged with respect to Equation (27). This LBGK approach is validated against a finite-difference solution in Section 5.1.

4.5. Scalar convection–diffusion equation with variable density

Examples for scalar convection–diffusion equations with variable density $\rho = \rho(\mathbf{x}, t)$ are the energy equation (39) or the species equations (40) in Section 5.1. A convection–diffusion equation for a variable ψ with a given source term $\dot{q}(\psi)$ in Cartesian coordinates $\alpha = \beta = x, y, z$ reads:

$$\partial_t(\rho\psi) + \partial_\beta \rho u_\beta \psi = \partial_\gamma \lambda \partial_\gamma \psi + \dot{q}(\psi) \tag{31}$$

The dependent variable $\rho \cdot \psi$ is defined here by the invariant moment

$$\rho \cdot \psi = \sum_i f_i = \sum_i F_i$$

The non-linear part $\sim u_\alpha u_\beta$ in the equilibrium distribution function equation (10) is neglected here, so the complete equilibrium distribution inclusive $F_{i,\mathrm{corr}}$ reads

$$F_i = t_p \psi \rho \left[1 + \frac{u_\alpha c_{i\alpha}}{c_s^2} \right] + \frac{t_p}{c_s^2}\,\lambda c_\gamma\, \frac{\partial_\delta \rho}{\rho} \left(\frac{c_{i\gamma} c_{i\delta}}{c_s^2} - \delta_{\gamma\delta} \right)$$

Again, the comparison with the equations of moments, Equations (20) and (21), yields the following relations for the source terms of the LBGK approach:

$$\begin{aligned} s_i^{(1)} &= t_p \dot{q}(\psi) \\ \lambda/\rho &= \delta t c_s^2 \left(\frac{1}{\Omega} - \frac{1}{2} \right) \end{aligned} \tag{32}$$

The convection–diffusion equation can also be formulated in a axisymmetric coordinate system in a similar way as done for Equation (24).

One has to remark here that the use of LBGK approaches for solving scalar convection–diffusion equations is of advantage if complex boundaries are present, these approaches increase, however, the storage requirements compared to a finite-difference solution of the macroscopic equations. Therefore, as a compromise, the flow equations are usually solved with advantage by the LBGK method while additional scalar equations are solved by finite-difference solutions. Examples are the computations in Section 5.1 or in Reference [16].

4.6. Poisson and Laplace equations

The present LBGK concept enables in a similar way the representation of scalar equations of the type of Poisson or Laplace equations for a potential function ϕ_α

$$\frac{\partial^2 \phi_\alpha}{\partial x_\beta^2} = -RS_\alpha \tag{33}$$

where RS_α is a prescribed right-hand side. LBGK solutions of this type of equations are presently used to compute electric or magnetic force potentials over complex geometries, [18]. The potential ϕ_α, interpreted as a component of a vector potential with $\alpha = 1,2,3$, is defined as the first invariant moment

$$\phi_\alpha = M_{1\alpha} = \sum_i f_i c_{i\alpha} = \sum_i F_i c_{i\alpha}, \quad \alpha = 1,2,3 \tag{34}$$

A linear equilibrium distribution is defined by

$$F_i(t,\mathbf{x}) = t_p \left[1 + \frac{\phi_\alpha c_{i\alpha}}{c_s^2}\right]$$

The source terms in Equation (7) are determined as

$$s_i^{(1)} = 0 \quad \text{and} \quad \delta t s_i^{(2)} = t_p \left(1 - \frac{\Omega}{2}\right) c_{i\alpha} \left(2\partial_\alpha M_0 + \frac{\delta t}{\Omega} RS_\alpha\right)$$

The term $\partial_\alpha M_0$ corrects non-equilibrium effects, since the zeroth order moment M_0 of the non-equilibrium distribution is different from the equilibrium value and is defined as

$$M_0 = \sum_{p,i} f_{pi} \neq \sum_{p,i} F_i \tag{35}$$

Neglecting the temporal derivatives in Equation (18) and taking into account Equation (35), one can derive a kind of continuity equation in the form

$$\partial_\alpha \phi_\alpha = \frac{\Omega}{\delta_t}(1 - M_0) \tag{36}$$

The corresponding equation of the first moment M_1 is derived in a similar way as Equation (21) by a multiplication with $c_{i\alpha}$ and summation over all distributions. The equation for the first moment yields the desired Poisson equation (33) for the potential equation (34) after including Equation (36). The LBGK solution results in three potentials ϕ_α for $\alpha = 1,2,3$ in 3-D, each

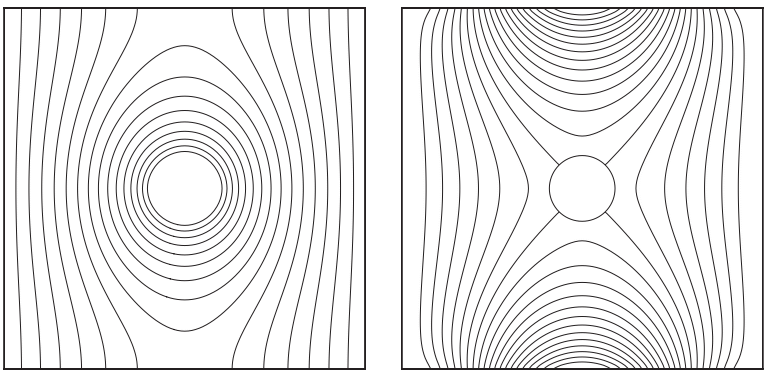

Figure 3. Comparison between a lattice-BGK and a finite-difference solution for an electrical potential using Dirichlet (left) or gradient boundary conditions (right) on the cylinder.

satisfies a Poisson equation of type Equation (33). It looks therefore like a result for vector potentials, but the potentials are not independent here through the coupling over boundary conditions. Thus only one component is usually used. Figure 3 shows a comparison between solutions of the LBGK method and of a finite-difference method for an electrical potential using Dirichlet (left) or gradient boundary conditions (right) on the cylinder boundary. The results are more or less identically but the computational time of the LBGK approach is nearly a factor two larger than a finite-difference solution for the Laplace equation on Cartesian meshes. The essential advantage of the LBGK solution for these type of equations, however, is seen in the capability of dealing with complex geometries in a relatively simple way, as used in Section 5.2 for filter surfaces with deposited particles.

5. TEST CASES

5.1. Axisymmetric chemical reactor

An axisymmetric chemical reactor configuration, based on an experimental arrangement for the generation of nano-particles in Reference [19], was designed to validate and to compare solutions of the new LBGK approach with results of a pressure relaxation method using finite differences. The same geometrical, physical and chemical data and the same meshes, as well, are used for both solution concepts. The model reactor is sketched in Figure 4.

The governing equations, describing the chemical reacting flow, are presented in the following for Cartesian coordinates ($\theta = 0$) and for an axisymmetric system ($\theta = 1$):

- Continuity equation:

$$\partial_t \rho_{\text{mix}} + \partial_\alpha(\rho_{\text{mix}} u_\alpha) = -\frac{\theta}{r}\,\rho_{\text{mix}}\,u_r \tag{37}$$

where ρ_{mix} the mixture density.

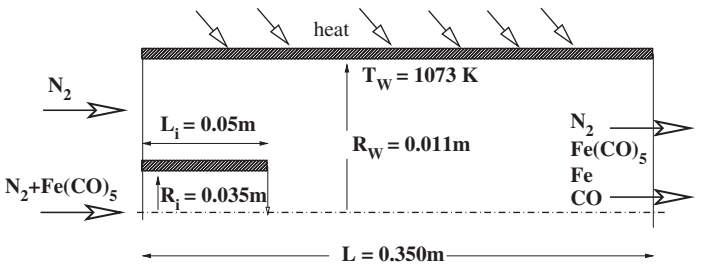

Figure 4. Model arrangement of the axisymmetric, chemical test reactor.

- Momentum equations:

$$\partial_t \rho_{\text{mix}} u_\alpha + \partial_\beta (\rho_{\text{mix}} u_\beta u_\alpha) + \partial_\alpha p^{(2)} - \partial_\beta \mu \left(\partial_\beta u_\alpha + \partial_\alpha u_\beta - \frac{2}{3} \delta_{\alpha\beta} \partial_\gamma u_\gamma \right)$$
$$= \frac{\theta}{r} \left(-\rho_{\text{mix}} u_r u_\alpha + \mu \left(\delta_{\alpha x} (\partial_r u_x + \partial_x u_r) + \delta_{\alpha r} 2 \cdot \partial_r \left(\frac{u_r}{r} \right) \right) \right) \tag{38}$$

  The pressure is split in the thermodynamic pressure $p^{(0)}(t)$, which is assumed here as a constant, and in the hydrodynamic pressure $p^{(2)}$, ensuring mass conservation.
- Energy equation:

$$\rho_{\text{mix}} c_p (\partial_t T + u_\beta \partial_\beta T) - \partial_\gamma \lambda \partial_\gamma T - \rho_{\text{mix}} \sum_k h_k w_k - \frac{\mathrm{d} p_{th}(t)}{\mathrm{d}t} = \frac{\theta}{r} \lambda \delta_r T \tag{39}$$

  where w_k and h_k are the production rate and the heat of formation of the reacting species.
- Species equations for $k = 1, 2, \ldots, k_{\max}$ species:

$$\rho_{\text{mix}} (\partial_t \xi_k + u_\beta \partial_\beta \xi_k) - \partial_\gamma (\rho D)_{kl} \partial_\gamma \xi_k + \rho_{\text{mix}} w_k = \frac{\theta}{r} \rho D_{kl} \delta_r \xi_k \tag{40}$$

  where $\xi_k = \rho_k / \rho_{\text{mix}}$ is the mass fraction of the kth species and D_{kl} a binary diffusion coefficient. The number of species is $k_{\max} = 4$ for the reaction described below.
- Mixture density $\rho_{\text{mix}}(T, \xi_i)$

$$\rho_{\text{mix}} = \sum_k \rho_k = \frac{p^{(0)}(t)}{R_{\text{mix}}(\mathbf{x}, t)\, T(\mathbf{x}, t)} \quad \text{with} \quad R = \sum_k \frac{\xi_k}{W_k} \tag{41}$$

The chemical reaction under investigation is used for the generation of iron particles in gas phase reactions. The global reaction used in the test cases reads:

$$\text{Fe(CO)}_5 \rightarrow \text{Fe} + 5\text{CO}$$

with the forward reaction speed of $k = 1.93 \times 10^9 (1/s) \exp[-(72 \times 10^6 / RT)]$. Detailed reaction data are taken from Reference [20]. The reactor, as sketched in Figure 4, consists of a cylindrical vessel of length L with a heated outer wall of radius R_{W} and an inner pipe of radius R_{i} and length L_{i}. The reacting precursor gas $Fe(CO)_5$ is feed in through the inner pipe together with an inert gas N_2. The precursor decomposes under external heat to Fe-atoms,

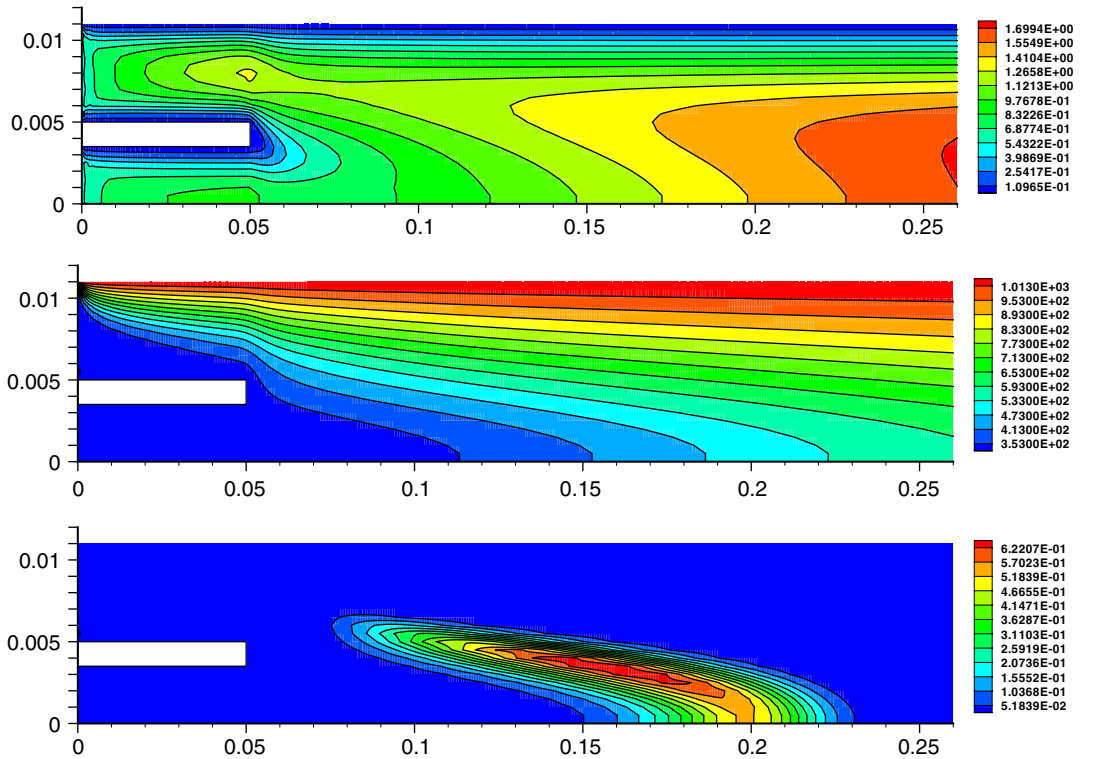

Figure 5. Lattice-BGK solutions for axisymmetric, reactive flow in the reactor as sketched in Figure 4. The grid resolution is 1201×43 grid points. From top to bottom: colours of constant axial velocity, temperature and reaction rate of $Fe(CO)_5$.

which grow along their paths by nucleation and coagulation to nano-particles, which is the matter of a separate investigation.

The underlying grid is a uniform Cartesian-like grid of constant radial and axial step-sizes. The number of grid points in axial and radial direction are 1201×46 for the following results. The outer walls and the axis coincide with grid lines, thus boundary conditions have to be prescribed directly on the nodes. The boundary conditions are formulated identically for both the finite-difference and LBGK solutions, as well. No-slip conditions for the velocities and zero normal pressure gradients are applied at the walls. The temperature at the outer wall is assumed to be 1073 and 300 K at inner walls. The terms proportional $1/r$ on the axis are expanded in the limit $r \to 0$ assuming axial symmetry and are approximated by finite differences. The boundary conditions are implemented for the LBGK method in form of equilibrium functions using the same macroscopic boundary values as for the finite-difference solutions.

Figure 5 shows three typical results for colours of constant values of axial velocity, of temperature and of the reaction rate in the plane of axial and radial coordinates. The figures do not differ remarkably for LBGK and finite-difference solutions, thus the results from LBGK computation are plotted here.

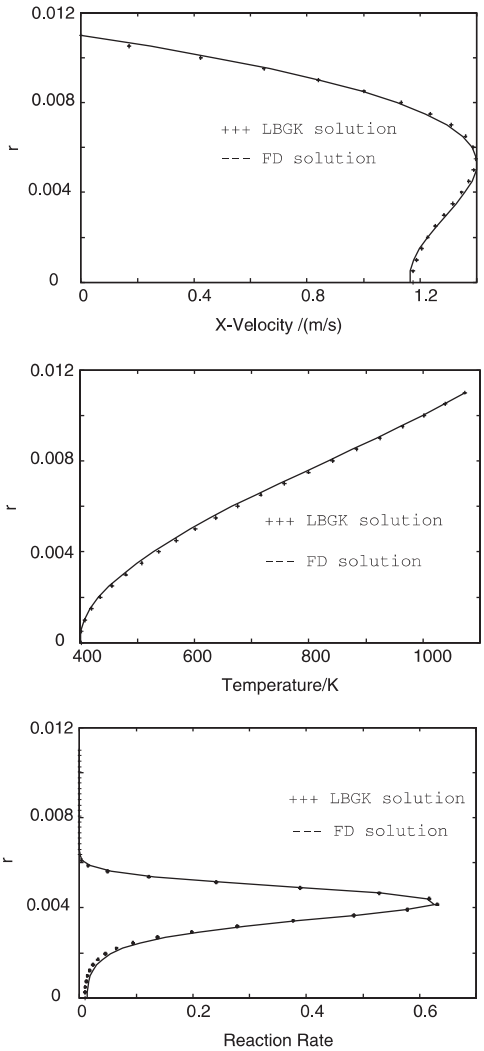

Figure 6. Comparisons between lattice-BGK solutions (crosses) and finite-difference solutions (full lines) for the same grid resolution of 1201×43 grid points in a cut $x = 0.175$ m of the axisymmetric reactor as sketched in Figure 4. Plotted are the axial velocity (top), the temperature (middle) and the reaction rate of $Fe(CO)_5$ (bottom) versus radius.

Quantitative comparisons are made in Figure 6 between solutions of the axisymmetric variant of the LBGK method and a corresponding finite-difference method with pressure relaxation. LBGK results mean here that the LBGK method is applied to the flow equations, i.e. to the continuity equation (37) and the momentum equations (38), while the energy and species equations are solved by explicit finite-difference schemes. Finite-difference solutions mean that all equations are solved by finite-difference schemes. Figure 6 shows radial profiles of the axial velocity, of the temperature and of the reaction rate of $Fe(CO)_5$ in a cut at an

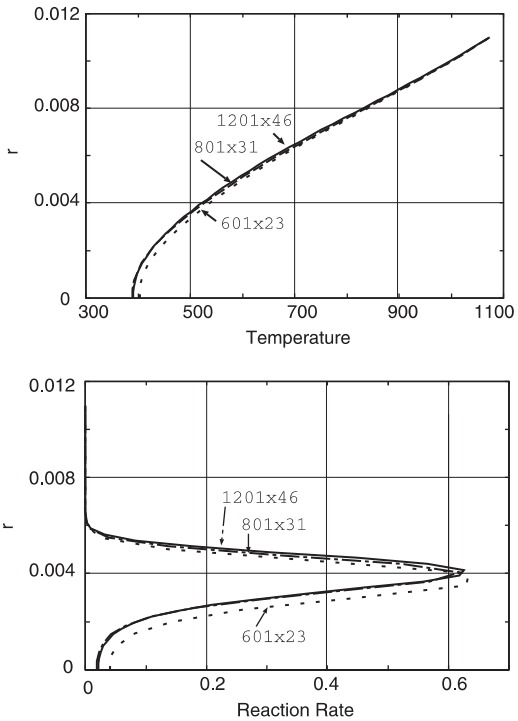

Figure 7. Comparison between lattice-BGK solutions for different grid resolutions with 1201×43, 801×31 and 601×23 grid points. Plotted are the temperature (top) and the reaction rate of $Fe(CO)_5$ (bottom) versus radius.

axial position of $x = 0.175$ m. The finite-difference solution is plotted as full line, the LBGK solution is marked by crosses. The differences are minor as expected.

A simple test of grid dependence is shown in Figure 7 for radial profiles of temperature (top) and of the reaction rate of $Fe(CO)_5$ (bottom) versus radius, similar as in Figure 6. However, comparison is made here between LBGK solutions using different grid resolutions with 1201×43, 801×31 and 601×23 grid points. The convergence behaviour is satisfactory, i.e. the coarsest grid with only 23 nodes in radial direction results in a remarkable difference compared to the results on finer grids, which seem to converge in one profile. A more detailed investigation of grid dependence of LBGK methods was performed by the authors in Reference [9]. It could be shown there that the LBGK method even with grid refinement is essentially second order accurate in space $O(\delta x^p)$ with an exponent p between $p = 1.83$ and 2.44 determined by the formula of Richardson.

5.2. Particle transport and deposition

Another interesting application of LBGK methods is the numerical investigation of transport and deposition of particles on filter surfaces [18, 21]. The LBGK method is coupled in this study with a Lagrangian particle (Monte-Carlo) methods. The particle Monte-Carlo method for computing the translatory motion discrete particles with drag force $\mathbf{F}_{\text{drag}}$, external force $\mathbf{F}_{\text{ext}}$ and

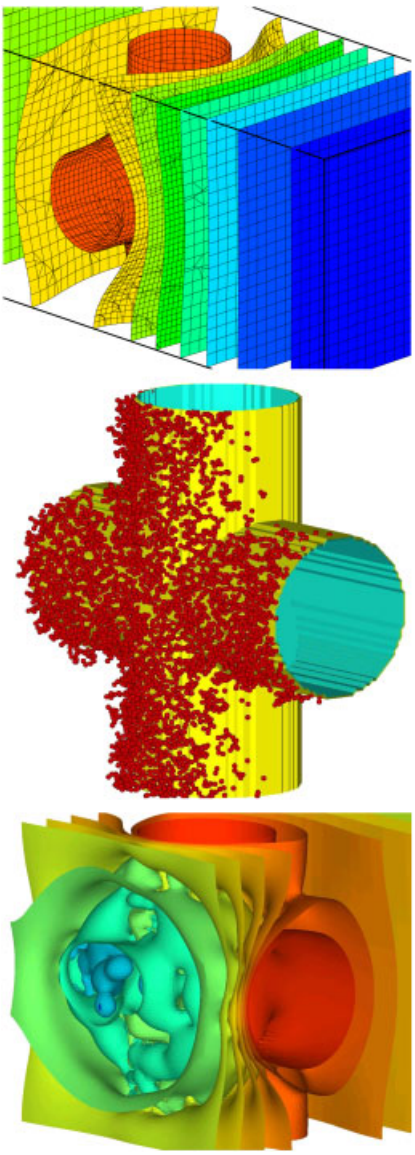

Figure 8. Planes of constant electrical potential around periodical, crossing filter fibres of diameter $d_f = 65\,\mu m$ with inflow velocity $U_{in} = 0.1\,m/s$ and electric field strength of $E = 300\,kV/m$ (top), layers of deposited nano-particles of $d_p = 10\,nm$ (mid) and planes of constant electrical potential, disturbed by deposited particles (bottom).

random forces $\mathbf{F}_{random}$ due to Brownian diffusion reads in a short form

$$m_p \frac{d\mathbf{v}_p}{dt} = \mathbf{F}_{drag} + \mathbf{F}_{ext} + \mathbf{F}_{random} \quad \text{and} \quad \frac{d\mathbf{r}_p}{dt} = \mathbf{v}_p \tag{42}$$

A set of three additional equations for the angular momentum with corresponding external and random torques has to be considered in addition, if magnetic particles and interactions are taken into account.

The solution of the problem requires the knowledge of the flow field for the drag and of the potential fields for determining external, electrical or magnetic forces $\mathbf{F}_{\text{ext}}$ or torques $\mathbf{T}_{\text{ext}}$. The geometrical boundaries are relatively complex in both cases due to the complex, three-dimensional filter geometries but also due to the irregular surfaces caused by particles deposited on the surfaces. An advantage of LBGK methods is that such complex boundaries conditions for the fluid flows or the electric field are easily treated by LBGK methods, as derived in References [7, 8]. The three-dimensional flow field of an incompressible fluid is computed here by the corresponding LBGK method, described in Section 4.1. The electric or scalar, magnetic potentials are determined by a Laplace equation, solved by a LBGK methods as described in Section 4.6. The solution of the Laplace equation, using the LBGK method, has found to be not much faster than a solution with usual iterative, finite-difference methods, but has shown to be more flexible for complex boundary conditions.

A demonstrative example for particle transport and deposition on filters under electrical forces with LBGK solutions for the flow field and the electrical field is shown in Figure 8. The left figure in Figure 8 shows planes of constant, undisturbed (by particles) electrical potential around the filter. The charge of the particles has the opposite sign of the charge of the filter fibre, so they are attracted by the filter. If a particle touches the filter surface or a particle already deposited, it deposits and exchanges its charge. The middle figure in Figure 8 gives an impression of the layers of deposited particles on the filter. Since the deposited particles change their charge, the surface having the constant potential of the undisturbed filter, grows and becomes irregular. The new boundary conditions are taken into account in the computation of the electrical field, which again influences the transport and deposition of the succeeding particles. The iterative re-computation is repeated after several hundred of time steps. The right figure in Figure 8 represents the equi-potential planes again after a certain computation time, but with the consideration of changed boundary conditions due to deposited particles.

6. CONCLUSIONS

Aim of the present study is an extension of the lattice-BGK concept to more general applications but to preserve the favourable properties of this gas-kinetic concept on isotropic Cartesian-like meshes. Extensions are made in this study by introducing additional free parameters to the LBGK formulation, which are determined then by comparisons of the resulting moment equations with the flow equations under consideration. Examples of LBGK extensions are given for the Navier–Stokes equations at low Mach numbers in Cartesian or axisymmetric coordinates with constant or variable density, for scalar convection–diffusion equations and for Poisson equations. The applicability of this LBGK concept is demonstrated by the computation of chemically reacting flow in an axisymmetric reactor and by the simulation of particle transport and deposition. Comparisons with finite-difference solutions and a check of the grid dependence have confirmed the applicability of this concept. The win in CPU-time compared to the finite-difference solutions was (only) a factor of about two to five in the present numerical experiments, but without any optimization and parallelization. Doing the latter, a much better performance is expected for LBGK methods because their granular algorithm enables nearly optimal parallelization.

The gas-kinetic, LBGK model promises therefore a number of advantages against conventional finite-difference or finite-volume methods for the macroscopic equations.

- The present modifications extends the applicability of the LBGK methods.
- The method acts like a Cartesian grid solver, which makes grid generation much easier. Drawbacks in anisotropic flow fields are removed or reduced by local grid refinement.
- The algorithm is simple and granular, well suited for efficient parallelization.
- The molecular boundary formulation is well suited for complex geometries.
- The conceptual, small time steps of the LBGK methods, scaled with the speed of sound, make the LBGK methods efficient for mathematically stiff flow problems.
- The LBGK concept avoids costly pressure relaxation for zero or low Mach numbers.

ACKNOWLEDGEMENTS

This investigation was supported by the German Research Society (DFG).

REFERENCES

1. Frisch U, Hasslacher B, Pomeau Y. Lattice gas automata for the Navier–Stokes equations. *Physical Review Letters* 1986; **56**:1506.
2. McNamara G, Zanetti G. Use of the Boltzmann equation to simulate lattice-gas automata. *Physical Review Letters* 1988; **61**:2332.
3. Higuera F, Succi S, Benzi R. Lattice gas dynamics with enhanced collisions. *Europhysics Letters* 1989; **9**:345.
4. Higuera F, Jimenez J. Boltzmann approach to lattice gas simulation. *Europhysics Letters* 1989; **9**:663.
5. Qian YH, d'Humiéres D, Lallemand P. LBGK models for Navier–Stokes equations. *Europhysics Letters* 1992; **17**:479–484.
6. Chen H, Chen D, Matthaeus W. Recovery of the Navier–Stokes equations through a lattice gas Boltzmann equation method. *Physical Review A* 1992; **45**:5339–5342.
7. Filippova O, Hänel D. Grid refinement for lattice-BGK models. *Journal of Computational Physics* 1998; **147**:219.
8. Filippova O, Hänel D. Boundary fitting and local grid refinement for lattice-BGK models. *International Journal of Modern Physics C* 1998; **9**:N8.
9. Filippova O, Hänel D. Acceleration of lattice-BGK schemes with grid refinement. *Journal of Computational Physics* 2000; **165**:407–427.
10. Peng G, Xi H, Duncan C, Chou SH. Finite volume scheme for the lattice Boltzmann method on unstructured meshes. *Physical Review E* 1999; **59**:4675–4682.
11. Lee T, Lin CL. A characteristic Galerkin method for discrete Boltzmann equation. *Journal of Computational Physics* 2001; **171**:336–356.
12. Lantermann U, Hänel D, Kaiser R. Finite volume-based lattice Boltzmann method for general grids. In *Finite Volumes for Complex Applications III*, Herbin R, Kröner D (eds). Hermes Penton Ltd.: 2002; 374–380.
13. Majda A, Sethian J. The derivation and numerical solution of the equations for zero Mach number combustion. *Combustion Science and Technology* 1985; **42**:185–205.
14. Choi YH, Merkle CH. The application of preconditioning in viscous flows. *Journal of Computational Physics* 1993; **105**:207–223.
15. Hänel D. *Molekulare Gasdynamik* (1st edn) (in German). Springer: Berlin, Heidelberg, 2004.
16. Filippova O, Hänel D. A novel lattice-BGK approach for low Mach number combustion. *Journal of Computational Physics* 2000; **158**:139–145.
17. Halliday I, Hammond LA, Care CM, Good K, Stevens A. Lattice Boltzmann equation hydrodynamics. *Physical Review E* 2001; **64**:011208.
18. Hänel D, Lantermann U. Particle-Monte-Carlo and lattice Boltzmann methods for simulations of gas-particle flows. *Computer and Fluids*, 2006, in press.
19. Special research program at University of Duisburg SFB 445: '*Nano-particles from the gas phase*'. Granted by Deutsche Forschungsgemeinschaft DFG, 1999–2004.
20. Rumminger MD, Reinelt D, Babushok D, Linders GT. Numerical study of the inhibition of premixed and diffusion flames by iron penta carbonyl. *Combustion and Flame* 1999; **116**:207–219.
21. Hänel D, Lantermann U. Simulation of particle transport and deposition. In *Traffic and Granular Flow* '03, Hoogendorn SP, Luding S, Bovy PH, Schreckenberg M, Wolf D (eds). Springer: Berlin, Heidelberg, New York, 2005; 503–513.

